

A novel segmentation method for breast ultrasound images based on neutrosophic I-means clustering

Juan Shan, H. D. Cheng, and Yuxuan Wang

Citation: [Medical Physics](#) **39**, 5669 (2012); doi: 10.1118/1.4747271

View online: <http://dx.doi.org/10.1118/1.4747271>

View Table of Contents: <http://scitation.aip.org/content/aapm/journal/medphys/39/9?ver=pdfcov>

Published by the [American Association of Physicists in Medicine](#)



3D SCANNER

 **SUN NUCLEAR**
corporation

3D SCANNER™
View Our New Video Series:
Different by Design: 3D SCANNER Advantages

 **Do**
DOSIMETRY

 Watch the Videos Now! 

A novel segmentation method for breast ultrasound images based on neutrosophic I-means clustering

Juan Shan,^{a)} H. D. Cheng,^{b)} and Yuxuan Wang^{c)}

Department of Computer Science, Utah State University, Logan, Utah 84322

(Received 16 January 2012; revised 6 August 2012; accepted for publication 7 August 2012; published 29 August 2012)

Purpose: Fully automatic and accurate breast lesion segmentation is an essential and challenging task. In this paper, the authors develop a novel, effective, and fully automatic method for breast ultrasound (BUS) image segmentation.

Methods: The segmentation method utilizes a novel phase feature to improve the image quality, and a novel neutrosophic clustering approach to detect the accurate lesion boundary. First, a region of interest is generated to cut off complex background. After speckle reduction, an enhancement algorithm based on phase in max-energy orientation (PMO) is developed to further improve the image quality. The PMO is a newly proposed 2D phase feature obtained by filtering the image in the frequency domain and calculating the phase accumulation in the orientation with maximum energy. Finally, the authors propose a novel clustering approach called neutrosophic I-means (NLM) to detect the lesion boundary. NLM is a generalized clustering method that can be used to solve other clustering problems as well. In this paper, NLM is used to segment images with vague boundaries, and to deal with uncertainty better. To evaluate the performance of the proposed method, the authors compare it with the traditional fuzzy c-means clustering, active contour, level set, and watershed-based segmentation methods, using a common database. Radiologist's manual delineations are used as the golden standards. Five assessment metrics are utilized to evaluate the performance from different aspects. Both accuracy and efficiency are analyzed. Sensitivity analysis is also conducted to test the robustness of the proposed method.

Results: Compared with the other methods, the proposed method generates the most similar boundaries to the radiologist's manual delineations (TP rate is 92.4%, FP rate is 7.2%, and similarity rate is 86.3%; Hausdorff distance is 22.5 pixels and mean absolute distance is 4.8 pixels), with efficient processing speed (averagely 9.8 s per image). Sensitivity analysis shows the robustness of the proposed method as well.

Conclusions: The proposed method is a fully automatic segmentation method for BUS images that can generate accurate lesion boundaries even for complicated cases. The fast processing speed, robustness, and accuracy of the proposed method suggest its potential applications in clinics. © 2012 American Association of Physicists in Medicine. [<http://dx.doi.org/10.1118/1.4747271>]

Key words: automatic segmentation, breast ultrasound (BUS) image, contrast enhancement, neutrosophy

I. INTRODUCTION

Breast cancer is the second leading cause of death for women all over the world and more than 8% women will suffer this disease during their lifetime.¹ According to cancer statistics 2010, it is estimated that there are 209 060 new cases of breast cancer and approximately 40 230 deaths in the United States.² Ultrasound is a useful diagnostic tool for breast cancer which can increase cancer detection rate by 17%,³ and it is widely used in clinic due to the fact that it is noninvasive, practically harmless, portable, and cost effective.¹

Since ultrasound (US) imaging is much more operator-dependent than mammography, reading ultrasound image requires well-trained and experienced radiologists. Further, even well-trained experts may have a high interobserver variation rate; therefore, computer-aided diagnosis (CAD) has been studied to help radiologists in making accurate diagnoses. One advantage of a CAD system is that it can ob-

tain some features, such as computational features and statistical features, which cannot be obtained visually and intuitively by medical doctors. Another advantage is that CAD can minimize the operator-dependent nature inherent in ultrasound imaging and make the diagnosis process reproducible. It should be noticed that research of CAD is not for eliminating radiologists, rather the goal is to provide doctors a second opinion and help them to increase diagnosis accuracy, reduce biopsy rate, and save their time and effort.

Segmentation is an important step of CAD systems. Both automation and accuracy of segmentation are crucial for CAD systems. A fully automatic CAD can minimize the effect of the operator-dependent nature inherent in ultrasound imaging, make the diagnosis process reproducible and reduce the observation error of human. Accuracy of segmentation is important because many crucial features¹ for discriminating benign and malignant lesions are based on the contour, shape,

and texture of the lesion (ACR BI-RADS lexicon⁴). These features can be effectively extracted only after the lesion boundary is correctly detected. Thus, an accurate segmentation method is essential for accurate diagnosis. However, there are characteristic artifacts, such as attenuation, speckle, shadows, and signal dropout, which make the segmentation task complicated; these artifacts are due to the orientation dependence of acquisition that can result in missing boundaries. Further complications arise as the contrast between areas of interest is often low.⁵ How to conduct one of the oldest image processing tasks, image segmentation, for breast ultrasound (BUS), is still a challenging task.

Many efforts have been done in BUS image segmentation. Simple histogram thresholding or region-growing algorithm can find the preliminary lesion boundary.^{6,7} Although very fast, these methods cannot guarantee precise boundary detection since they are quite sensitive to noise. They can serve as an intermediate step to provide a rough contour⁶ or can be combined with postprocessing procedures such as morphological operations⁷ and disk expansion.⁸ Filtering techniques are also utilized for lesion detection. A radial gradient index (RGI) filtering technique for breast lesion detection was developed³ and a nonparametric wavelet model based on order statistics was utilized to distinguish tumor and normal tissue regions.⁹ Filtering techniques are good at detecting the rough location of a tumor region, but not good at finding the accurate boundary of a lesion. Machine learning methods^{10–12} can produce reasonable lesion contours. The disadvantage of machine learning methods is that the training process is relatively time-consuming and the performance depends on whether the test images and training images come from consistent platforms. Watershed-based approaches have shown promising performance for US image segmentation.¹³ used a Canny edge detector to detect the rough location of tumor and then employed watershed algorithm to further segment the lesion. The biggest challenge for such methods is oversegmentation; to address this problem, marker-controlled^{14,15} and cell competition^{16,17} watershed methods are developed. However, they cannot solve the oversegmentation problem completely.¹⁷ Model-based methods have strong noise-resistant abilities and are relatively stable at sonography demarcation. Commonly used models include level set,^{18,19} active contours,^{6,20–22} Markov random fields (MRF),^{23,24} etc. For model-based approaches, an energy function is formulated, and the segmentation problem is transformed as finding the minimum (or maximum) of the energy function. Calculating energy functions and reformulating the models are always time-consuming, especially, for complex BUS images; in addition, many models highly rely on prelabeled ROIs (regions of interest) or manually initialized contours, which impede the full automation of BUS image segmentation.

In this paper, we develop a novel and fully automatic lesion segmentation approach for BUS images. It consists of an automatic ROI selection method, a new contrast enhancement method, and a novel clustering method. Each of them serves as an intermediate step of the entire approach. The contributions of the paper are summarized below.

1. The approach achieves complete automation and accurate segmentation at the same time. For medical image segmentation, high accuracy requires more human intervention, and realizing full automation is often at the expense of accuracy. The proposed approach successfully resolves such dilemma.
2. An automatic ROI generation method is developed, which serves as the preprocessing step of the segmentation. The ROI is a relatively small rectangular region comparing with the original image. The further operations will be only conducted on the ROI. Cutting off the complicated background not only speeds up the segmentation process, but also improves the accuracy.
3. We develop an effective enhancement method for BUS images using phase information. Phase is frequently used as an edge detector, however, we find a new way to use phase (i.e., a novel phase feature) to reduce the granular effect of the BUS images and enhance the contrast between the lesion and the background. After applying the proposed enhancement method, the BUS images become more homogeneous; and contrast between lesion and background is greatly improved without overenhancement effect.
4. A novel clustering method, neutrosophic *l*-means (NLM), based on neutrosophy and fuzzy c-means (FCM) is developed. NLM has many potential applications as a generalized cluster. In this paper, it is applied to separate the lesion and the background of the BUS images to demonstrate its superiority. Neutrosophy is a new branch of philosophy to deal with uncertainty. Such ability is employed to segment the BUS images with vague boundaries. By defining neutrosophic components and incorporating indeterminate degree in the clustering process, NLM can handle pixels with intermediate intensity values effectively. The clustering process is not only decided by the distance to the cluster centers and the membership, but also by the indeterminate degree and neighborhood information.
5. In experiment section, sound and fair comparisons between the proposed method, FCM, and three other BUS image segmentation methods are conducted. The same database of 122 BUS images and comprehensive evaluation metrics are employed to compare the performances of different methods.

II. PROPOSED METHOD

The proposed segmentation method is composed of four steps that are all executed automatically: ROI generation, speckle reduction, contrast enhancement, and NLM clustering. Among the four steps, the ROI generation method, the contrast enhancement method, and NLM clustering are newly proposed here. The flowchart of the proposed method is shown in Fig. 1.

II.A. ROI generation

Since the BUS image contains a lot of different structures (connective tissue, fat, muscles, etc.)¹ and the lesion

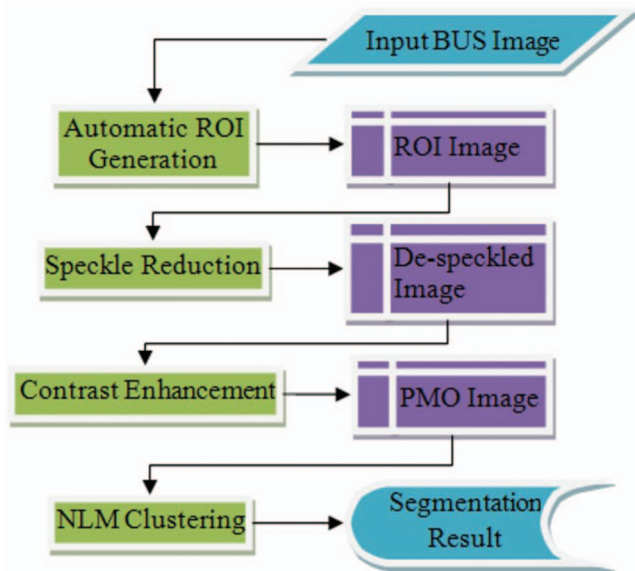


FIG. 1. Flowchart of the proposed method.

area is usually small compared to the entire image, finding a ROI is quite helpful for improving the speed and accuracy of segmentation. Many BUS image segmentation methods have been developed based on a manually selected ROI, but not on the whole image. Such requirement impedes full automation. In this section, we describe the development of an automatic ROI generation method that facilitates full automation of BUS image segmentation.

There are two typical ROI definitions: one defines ROI as a rough contour or initial contour of the lesion,^{6,19} while the other defines ROI as a rectangular region.^{7,25} In this paper, the automatically generated ROI is a rectangular region; only the redundant background is removed, and the lesion and nearby surrounding tissues are untouched. The ROI generation method consists of two steps: automatic seed point selection and region growing. Region growing is chosen because it is simple and fast. The lesion boundary detected by region growing method is usually not accurate for BUS images. However, the target here is only to locate the lesion roughly rather than to find the accurate boundary. Region growing fits our needs very well.

A seed point is the starting point for region growing. Its selection is important to the segmentation result. We employ the automatic seed point selection method developed in our previous work.²⁶ It is briefly described here. First, speckle reducing anisotropic diffusion (SRAD) (Ref. 27) is employed to remove speckle noise. Second, a self-adapted threshold selection mechanism is used to find a proper threshold to separate background and foreground. The selection process starts from the first local minimum in the histogram. Then the image is binarized using the current local minimum. If the ratio of the number of foreground pixels and the number of background pixels is less than 0.1, or none of the foregrounds intersects with the image center region (a window is about 1/4 size of the whole image and located at the image center), utilize the next local minimum and repeat this step. Otherwise, go to the next step. Delete the boundary-connected regions from

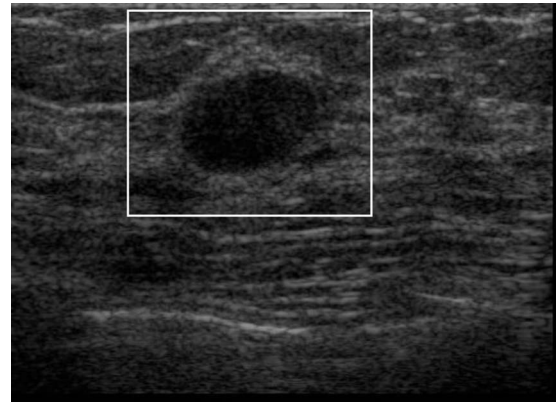


FIG. 2. Automatically generated ROI.

the ROI candidates. Then the candidates are ranked based on their eligibility scores. The one with the highest score is the winning region and the center of the region is selected as the seed point. For details, please refer to Ref. 26.

After a seed point is generated automatically, we employ a region growing method to obtain a preliminary lesion region. The basic criterion of region growing for simple segmentation task is to compare the intensity value of the new pixel v with the intensity mean of the current region, and if they are close enough, pixel v is added into the region. However, it is not enough to use only the intensity mean of the current region to control growing process for complicated images, such as BUS images. We find the stop criterion is related with both the intensity mean of the current region and the intensity mean of the entire image. The threshold is a dynamic value changed from image to image. Therefore, the following conditions are used to control the growing process. Let R represent the set containing all the pixels in the region, and p be a pixel in R . At the beginning, set R contains only the seed point S_0 . A pixel v is included in R , if $\exists p \in R$ and satisfies the following condition:

$$\left\{ G(v) \leq \max \left(\frac{\bar{M}}{b_2}, \min(b_1 \times \bar{m}, \bar{M}) \right) \right\} \\ \text{and } \{N(p) \cap N(v) \neq \emptyset\}, \quad (1)$$

where $G(v)$ is the intensity value of pixel v , \bar{m} is the intensity mean of region R , \bar{M} is the intensity mean of the entire image, and b_1 and b_2 are the parameters tuning the relationship between the stop criterion and the intensity means of the current region and the entire image. N denotes the type of connectivity of the neighborhood pixels around the pixel under consideration. The above operation proceeds until no more pixels satisfying Eq. (1) remain. In this work, we used eight-neighborhood connectivity, and $b_1 = 1.5$ and $b_2 = 1.6$ are determined by previous experiments using the entire dataset.²⁸

Based on the region growing result, a rectangular ROI is located from the original image. To make sure that the lesion is completely covered by the ROI, we let the rectangular region have a 50-pixel expansion surrounding the region growing result. For example, the size of the original BUS image in Fig. 2 is 372×508 pixels. The top left pixel of the entire image has coordinates (1, 1) and bottom right pixel of the entire image

has coordinates (372, 508). The lesion area generated from the region growing method is entirely covered in the rectangular region [56:148, 58:287], then the region [6:198, 108:337] is finally chosen as the ROI. In our experiment, the average processing time of the ROI generation for each case is about 2 s, using a 3.0 GHz Pentium processor (0.36 s for seed point selection and 1.61 s for region growing). For every image in the database, the ROI generation method can produce such a rectangular region that covers the lesion completely.

II.B. Speckle reduction and contrast enhancement

II.B.1. Speckle reduction

From this step, we will work on ROIs instead of entire BUS images. Apply the same speckle reduction method SRAD (Ref. 27) on ROIs to remove speckle noise. SRAD is used in the last section on the entire images for finding seed points. The reason we employ SRAD again is that SRAD generates better speckle reduction effect on ROIs than on entire images. An example of the intermediate result after applying SRAD on a ROI will be shown later.

II.B.2. Contrast enhancement

Local phase has been suggested as a robust feature for acoustic boundary detection.⁵ It characterizes different intensity features in terms of the shape of intensity profile rather than the intensity derivative. The most important advantage of the local phase is that it is invariant to image illumination and contrast, i.e., the local phase does not change no matter whether the contrast between foreground and background is low or high. This characteristic of local phase is very important and particularly useful for acoustic feature detection, since ultrasound images always have the inherent problems of low contrast that is also varied from image to image.

In this section, we explore a new 2D phase feature based on local phase and use it to improve the quality and contrast of BUS images, without amplifying the noise or overenhancement. It should be emphasized that the phase is referred to “local phase” in this paper. Local phase is defined for each position x in the spatial domain after the signal is convolved with an analyzing filter (such as the Log-Gabor filter). Conversely, the phase is obtained from fast Fourier transform (FFT) of a signal that is defined as the phase offsets of the sinusoidal basis functions in the decomposition.

To calculate the 1D local phase, a one-dimensional signal $I(x)$ is analyzed by a bank of Log-Gabor filters. The Log-Gabor transfer function is defined in the frequency domain,

$$G(\omega) = \exp\left(-\frac{(\log(\omega/\omega_0))^2}{2(\log(\kappa/\omega_0))^2}\right), \quad (2)$$

where κ is related to the bandwidth of the filter and ω_0 is the center frequency of the filter. The value κ/ω_0 ensures a constant shape-bandwidth ratio over the scales and is set as 0.55 to obtain a compromise between filters compact and avoid aliasing effect.²⁹

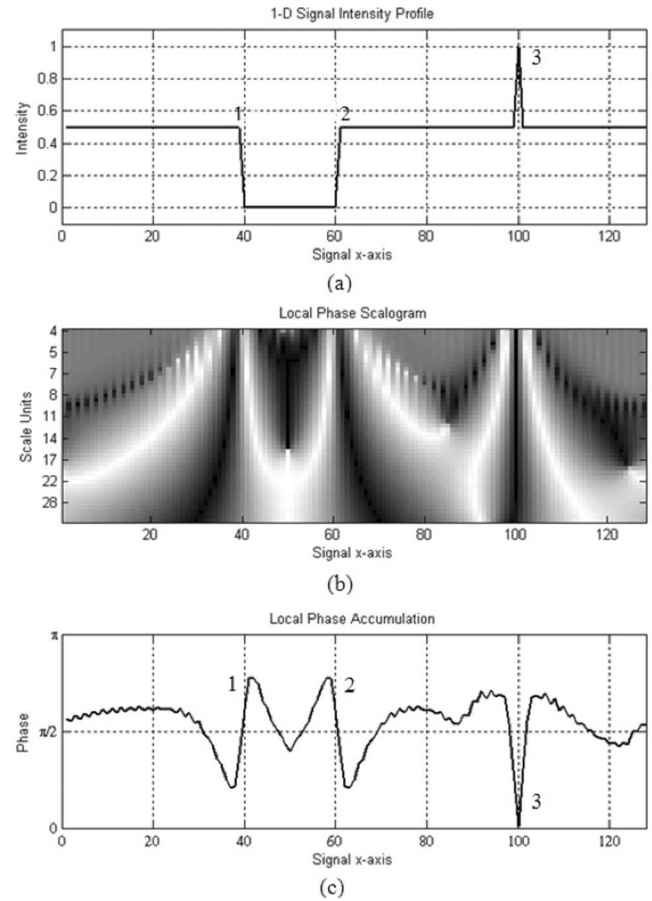


FIG. 3. (a) A 1D signal with step edges (1, 2) and intensity ridge (3). (b) Local phase scalogram. (c) LPA.

Let M_s^e and M_s^o denote the even and odd symmetric Log-Gabor filters in quadrature at scale s . The even and odd components of the signal at scale s can be approximated by

$$e(x, s) = I(x) * M_s^e, \quad o(x, s) = I(x) * M_s^o. \quad (3)$$

Then the local phase at scale s is obtained by

$$\text{phase}(x, s) = \|\tan^{-1}(e(x, s)/o(x, s))\|. \quad (4)$$

For a 1D signal, the local phases keep consistent at π for step edges and 0 for intensity ridge, after the phase values are scaled into range $[0, \pi]$. This is well illustrated in Fig. 3. Figure 3(a) is a 1D signal $I(x)$ with edges labeled as 1 and 2, and an intensity ridge is labeled as 3. In Fig. 3(b), the local phase scalogram is plotted for distance x along the signal over a range of scale s . Black is the 0 phase and white is the π . Observe that, for the step edges [labeled 1 and 2 in Fig. 3(a)], the corresponding phase values in Fig. 3(b) are consistent at π (shown as the thick bright white lines), within a certain scale range. For the intensity ridge [labeled 3 in Fig. 3(a)], the phase values in Fig. 3(b) are consistent at 0 (shown as the thick black line). Based on such observations, if accumulating all the local phases at different scales, the highest peaks should represent step edges and the lowest valley should represent the intensity ridge. Therefore, we define the local phase

accumulation (LPA) to capture such consistency,

$$\text{LPA}(x) = \frac{1}{n} \sum_{s=1}^n \text{phase}(x, s), \quad (5)$$

where n is the total number of scales, $\text{phase}(x, s)$ is the local phase defined in Eq. (4). Figure 3(c) plots the LPA with the step edges 1 and 2, and intensity ridge 3.

To extract phase feature of images, the above analysis needs to be extended from 1D to 2D. One way to extend a feature from 1D to 2D is to calculate that feature in a number of orientations, and integrate the information obtained from multiple orientations.

A bank of 2D Log-Gabor filters centered at different orientations is applied to the image in frequency domain. The 2D Log-Gabor filter in a given orientation θ_0 is defined as the 1D Log-Gabor filter multiplying a Gaussian orientation function,²⁹

$$G(\omega, \theta) = \exp - \left(\frac{(\log(\omega/\omega_0))^2}{2(\log(\kappa/\omega_0))^2} + \frac{(\theta - \theta_0)^2}{2\sigma_\theta^2} \right), \quad (6)$$

where σ_θ defines the spread of the Gaussian orientation function centered at θ_0 . In this work, six orientations ($0^\circ, 30^\circ, 60^\circ, 90^\circ, 120^\circ, 150^\circ$) are chosen because they achieve a good compromise between a complete coverage of the whole spectrum and efficiency. The orientation spread σ_θ is set as 30° .

Based on the observation on the 1D signal's phase scalogram, the local phases keep consistent at π for step edges and 0 for intensity ridges in a certain range of scales. LPA can pinpoint such consistency. In a 2D image, the local phase has similar characteristics. The only difference is that there are six LPAs since the image is filtered along six orientations. How to utilize the six phase features to obtain a single feature is our concern.

In previous works, a 2D phase feature is usually calculated through the summation of phase values in all the orientations. However, we find that the phase from the orientation corresponding to the maximum energy can provide a better image feature than the phase summation from all orientations. This is because unlike 1D signal, in an image, the edge has orientation information, and different parts of the edge or boundary might have different orientations. Therefore, the LPA in the direction of the edge might better characterize the structure than the summation of the LPAs in different orientations. Since local energy characterizes structural information, the orientation with the maximum local energy should mostly approximate the direction of an edge. Hence, we use the LPA obtained from the orientation with the maximum energy as the feature, which is named PMO (phase in max-energy orientation). For every pixel (i, j) in the image, PMO is defined as

$$\text{PMO}(i, j) = \text{LPA}_\rho(i, j), \quad (7)$$

$$\rho = \arg \max_{\theta=0^\circ, 30^\circ, 60^\circ, 90^\circ, 120^\circ, 150^\circ} \text{Eng}_\theta(i, j),$$

where LPA_ρ represents the matrix of local phase accumulation of all scales at orientation ρ , and Eng_θ represents the local energy in orientation θ . Local energy Eng_θ is calculated

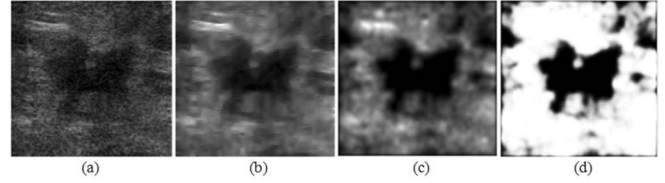


FIG. 4. (a) ROI. (b) Despeckled image by SRAD (Ref. 27). (c) PMO image after median filtering. (d) Enhanced PMO image.

by

$$\text{Eng}_\theta(i, j) = \sqrt{\left(\sum_{s=1}^n e(i, j; s) \right)^2 + \left(\sum_{s=1}^n o(i, j; s) \right)^2}, \quad (8)$$

where $e(i, j; s)$ and $o(i, j; s)$ are the even and odd components of the image pixel (i, j) after applying Log-Gabor filter at scale s ; and n is the total number of scales.

Several postprocessing steps are taken to further improve image quality: the PMO image is multiplied by the despeckled ROI image to homogenize the lesion region; then the resulting PMO image is filtered with a 5×5 median filter three times to homogenize the background. Since most of the pixels centralized in a low intensity range, a brightening function in Eq. (9) is employed to adjust the intensity values in range of $[0, 1]$. To further increase the contrast between lesion and background, an intensification function in Eq. (10) is employed to make the bright pixels brighter and dark pixels darker,

$$\text{PMO} = \begin{cases} 1 - 4(\text{PMO} - 0.5)^2 & 0 \leq \text{PMO} \leq 0.5 \\ 1 & 0.5 < \text{PMO} \leq 1 \end{cases}, \quad (9)$$

$$\text{PMO} = \begin{cases} 2\text{PMO} & 0 \leq \text{PMO} \leq 0.5 \\ 1 - 2(1 - \text{PMO})^2 & 0.5 < \text{PMO} \leq 1 \end{cases}. \quad (10)$$

Figure 4 shows the effect of the above operations. Figure 4(a) is the ROI generated from the original image automatically. Figure 4(b) is the despeckled image by the method given in Ref. 27. Figure 4(c) shows the PMO image after median filtering. Figure 4(d) shows the enhanced PMO image after brightening and intensification, which is the final result of the newly proposed contrast enhancement algorithm. The major advantage of PMO image [Fig. 4(c)] is that without much changing of the original intensity range, the local contrast between foreground and background is increased, and the texture of the image becomes smoother and clearer. Comparing Figs. 4(a)–4(c), we can see that the granular appearance inherent in US image is significantly reduced and the lesion boundary becomes more distinguishable. Further contrast enhancement operations [Eqs. (9) and (10)] provide a better distinction between lesion and background [Fig. 4(d)]. Please note that Eqs. (9) and (10) have good effect without overenhancement or amplifying the noise because the PMO image has already homogenized both the lesion area and background and greatly reduced the granular appearance. The average time for obtaining the enhanced PMO image is 2.6 s.

II.C. Lesion detection by NLM

In this section, we describe the newly proposed NLM clustering method that groups pixels into a lesion region and background. NLM is a generalized clustering method based on neutrosophy and fuzzy c-means. In this work, it is applied to image segmentation.

II.C.1. Fuzzy c-means

The FCM algorithm is a soft clustering method wherein a datum is allowed to belong to two or more clusters. The algorithm was first developed by Dunn in 1973 (Ref. 30) and improved by Bezdek in 1981.³¹ FCM is frequently used as clustering method for pattern recognition and machine learning. It is based on the minimization of the following objective function:

$$J_m = \sum_{i=1}^N \sum_{j=1}^C u_{ij}^m \|x_i - c_j\|^2, \quad 1 \leq m < \infty, \quad (11)$$

where m is a real number greater than 1, u_{ij} is the membership of x_i in cluster j , x_i is the i th datum, c_j is the center of cluster j , and $\|\cdot\|$ is any norm expressing the similarity between the datum and the center.

Fuzzy partitioning is carried out through iterative optimization of the above objective function, with the update of membership u_{ij} and cluster center c_j by

$$u_{ij} = \frac{1}{\sum_{n=1}^c (\| \frac{x_i - c_j}{x_i - c_n} \|)^{\frac{2}{m-1}}}, \quad (12)$$

$$c_j = \frac{\sum_{i=1}^N u_{ij}^m \cdot x_i}{\sum_{i=1}^N u_{ij}^m}. \quad (13)$$

The iteration will stop when

$$\max_{ij} \{ |u_{ij}^{(k+1)} - u_{ij}^{(k)}| \} < \varepsilon, \quad (14)$$

where ε is a predefined termination criterion between 0 and 1, and k is iteration step. The procedure converges to a local minimum or a saddle point of J_m .³¹

II.C.2. Neutrosophy

Neutrosophy is a new branch of philosophy that studies the origin, nature, and scope of neutralities, as well as their interactions with different ideational spectra.^{32,33} It is the base of neutrosophic logic that generalizes the fuzzy logic; and deals with paradoxes, contradictions, antitheses, and antinomies. Neutrosophic logic can solve some problems that cannot be solved by fuzzy logic.³³ For example, a case with suspected breast cancer was diagnosed by two doctors. They both diagnose the case as malignant with 80% assurance. However, the two doctors may have different level of background knowledge and experience. One is an expert, and another is a fresh doctor in this field. The same assurance should not have the same impact on the final diagnosis decision. There also exist a lot of other problems with indeterminacy such as weather

forecast, presidential election, sport games, etc. While fuzzy logic cannot handle the indeterminate conditions well,³⁴ neutrosophy is utilized and plays an important role to deal with such conditions.^{33,35,36}

Several works have been done in the field of neutrosophic image segmentation.^{33,35,37} Neutrosophic image segmentation³³ is a thresholding based method and neutrosophy is utilized to modify iteratively the threshold until the optimum threshold was obtained to separate image into background and foreground. Another method³⁵ combines neutrosophy with α -mean and β -enhancement operations to reduce the noise in gray images. The contribution of neutrosophy is that noise is greatly reduced in the image without blurring image boundary, hence, segmentation result is improved after noise reduction. When neutrosophy is applied to image segmentation, each pixel in the image is represented or described by three neutrosophic components: $t\%$ true, $f\%$ false, and $i\%$ indeterminate. The most important part of neutrosophy is that indeterminacy is taken into consideration. Since noise pixels in ultrasound image have high indeterminacy degree while edge pixels have low indeterminacy degree, the pixels in these two categories can be treated separately based on the indeterminacy degree – noise is reduced iteratively while edges are untouched or strengthened. The noise reduction effect was measured by the peak-signal-to-noise (PSNR) (Ref. 33) and signal-to-noise ratio (SNR) (Refs. 35). A neutrosophic approach³⁶ combines neutrosophy with the traditional watershed method and experiment results show that the neutrosophic watershed method improved the segmentation performance on both color images and US images, comparing with traditional watershed method. In this work, we explore a new application of neutrosophy by incorporating neutrosophic domain components with fuzzy c-means to better deal with data points with uncertainty. Clustering method is an unsupervised learning method which is adaptive and dynamic. The FCM algorithm is a generalization of classical K-means algorithm, and has many applications in machine learning, data mining, pattern classification, etc. The proposed NLM is a generalization of the FCM method that may find more applications in the related areas.

II.C.3. Definitions of neutrosophic components for BUS image segmentation

When applying neutrosophy to solve a specific problem, one must map the problem into the neutrosophic domain by defining the neutrosophic components. In this paper, the task is segmenting the lesion from the background. There are two clusters: foreground (lesion) and background. For this application, we define the neutrosophic pixel and its neutrosophic components as follows.

Definition 1 (Neutrosophic pixel).³³ Let X be a universe of the pixels, and a foreground set $A \subset X$. A pixel p is noted as $p(\hat{t}, \hat{i}, \hat{f})$, and belongs to A in the following way: it is $\hat{t}\%$ true in the foreground, $\hat{i}\%$ indeterminate, and $\hat{f}\%$ false, where \hat{t} varies in T , \hat{i} varies in I , and \hat{f} varies in F . T , I , and F are real standard sets with the range $[0, 1]$. For most applications, $\hat{t} + \hat{f} = 1$ and $0 \leq \hat{t} + \hat{f} + \hat{i} \leq 2$.

Definition 2 (Neutrosophic components for a pixel). In an image, the three neutrosophic components T , I , and F , for a pixel p at position (i, j) are defined as

$$T(i, j) = 1 - G(i, j), \quad (15)$$

$$I(i, j) = \text{BLUR}(i, j) * (1 - \text{EDGE}(i, j)), \quad (16)$$

$$\text{EDGE}(i, j) = \begin{cases} 1 & \text{if } p \text{ is on the edge by sobel edge detector} \\ 0 & \text{if } p \text{ is not on the edge by sobel edge detector} \end{cases} \quad (19)$$

where $G(i, j)$ is the intensity value normalized in $[0, 1]$. The motivation of the definition of neutrosophic components is discussed as follows.

We use the intensity value normalized in $[0, 1]$ and subtracted by 1 as the T value. This is because the lesion is dark and the background is bright. F value is the complement of T value. Although T and F are easily and simply defined, defining indeterminate set I is quite interesting and challenging. One should answer the following two questions: (1) what kind of pixels is hard to be determined (with high indeterminacy) according to a specific task, and (2) how to deal with such pixels better. Here, the task is separating pixels into two clusters: foreground and background. The foreground represents the lesion region, and the background includes all the pixels in the image except the lesion region. The image (actually the ROI) is composed of dark lesion region, bright background, dark noise regions in the background, and some regions with the intensity values in the middle of the intensities of the foreground and background. How to cluster such pixels with mediate intensities will greatly affect the segmentation accuracy. In order to assign high indeterminacy to these pixels, we calculate a BLUR matrix by Eq. (18). The pixels with intensity values around 0.5 have high indeterminacy values, and the pixels with intensity values near the extremes 0 or 1 have low indeterminacy values. However, not all the pixels with mediate intensity values should have high indeterminacy values. If a pixel with mediate intensity value lies on lesion's edge, the pixel should not have a high indeterminate value. Otherwise, the edge will be blurred since we use neighborhood mean to replace the intensity value of a pixel with high indeterminacy. Therefore, we calculate an EDGE matrix using Sobel edge detector, where the pixels on sharp edges are equal to 1 and other pixels are assigned 0. By multiplying BLUR and $(1 - \text{EDGE})$, only the pixels with mediate values and not on edges have high indeterminate values.

The second question is how to deal with the pixels having high indeterminacy. Here, we use the neighborhood mean to replace the value of the pixel with high indeterminacy,

$$G(i, j) = \frac{1}{w \times w} \sum_{s=i-w/2}^{i+w/2} \sum_{t=j-w/2}^{j+w/2} G(s, t), \quad (20)$$

$$F(i, j) = 1 - T(i, j), \quad (17)$$

where

$$\text{BLUR}(i, j) = \begin{cases} 2(1 - T(i, j)) & T(i, j) \geq 0.5 \\ 2T(i, j) & T(i, j) < 0.5 \end{cases}, \quad (18)$$

where w is the window size and $G(i, j)$ is the intensity value. If we repeat the process, an indeterminate pixel inside a lesion will be gradually integrated into the lesion region, while an indeterminate pixel in the background will be gradually assimilated into the background. Notice that we only apply Eq. (20) for the pixels with high indeterminacy. Intensity value of the pixel with low indeterminacy will not change. The threshold to distinguish high and low indeterminacies will be discussed in Sec. IV.C.

II.C.4. Neutrosophic I-means

Based on fuzzy c-means and the neutrosophic image defined above, a new clustering method, NLM, is proposed. NLM is composed of the following steps:

1. Initialize membership matrix $U^{(k)} = [u_{xy}]$; $k = 0$. Here x is the pixel index, y is the cluster index, and k is the iteration number.
2. $k = k + 1$. At the k th iteration, calculate $T^{(k)}$, $I^{(k)}$, and $F^{(k)}$ for image $G^{(k)}$ by using Eqs. (15)–(17), and transform $T^{(k)}$ and $I^{(k)}$ into vectors VT and VI .
3. Calculate the center vector $L^{(k)} = [l_q]$ using $U^{(k)}$, VT and VI ,

$$l_y = \frac{\sum_{x=1}^N u_{xy}^m \cdot (1 - VI_x) \cdot VT_x}{\sum_{x=1}^N u_{xy}^m \cdot (1 - VI_x)}, \quad (21)$$

where m is the membership parameter and N is the total number of pixels in the image. Here, the indeterminate degree VI is used to control a pixel's contribution to the cluster centers. If a pixel has a high indeterminate value, its contribution to all cluster centers is reduced. If a pixel has a low indeterminate value, its contribution to the cluster centers is decided by its membership u_{pq} .

4. Update membership matrix $U^{(k+1)} = [u_{xy}]$ by

$$u_{xy} = \frac{1}{\sum_{d=1}^L \left(\frac{\|VT_x - l_y\|}{\|VT_x - l_d\|} \right)^{\frac{2}{m-1}}}, \quad (22)$$

where L is the number of clusters.

5. Update image $G^{(k+1)}$ by

$$G^{(k+1)} = \begin{cases} G^{(k)} & \text{if } I^{(k)} < \lambda \\ G^{(k)} & \text{if } I^{(k)} \geq \lambda \end{cases}, \quad (23)$$

$$G^{(k)}(i, j) = \frac{\sum_{s=i-w/2}^{i+w/2} \sum_{t=j-w/2}^{j+w/2} G^{(k)}(s, t)}{w^2}, \quad (24)$$

where w is the size of the window, (i, j) is the pixel at the center of the window, and λ is the indeterminacy threshold.

6. If $1\|U^{(k+1)} - U^{(k)}\| < \varepsilon$, stop; otherwise go to step 2.

In this work, $L = 2$ since there are two clusters; $m = 2$, $w = 5$, and $\lambda = 0.1$ are determined by experiments on the entire dataset. The output binary image is obtained by

$$B(i, j) = \begin{cases} 1 & \text{If foreground membership } u_{x0} > \text{background membership } u_{x1} \\ 0 & \text{Otherwise} \end{cases}. \quad (25)$$

Time complexity of NLM is $k \cdot O(\text{Row} \times \text{Col})$, where k is the iteration number and $\text{Row} \times \text{Col}$ is the image size. The average processing time of the NLM algorithm is 5.2 s.

III. RESULTS

To validate the proposed method, we compare it with other segmentation methods. The best way to make a fair comparison among segmentation methods is to use a benchmark and evaluate the methods by a commonly accepted criterion. Unfortunately, there is no public-accessible benchmark and no universally accepted evaluation criterion yet. Therefore, we compare the methods using our own database, and use comprehensive evaluate metrics (five metrics are used here), to provide an overall comparison from different aspects.

III.A. Database

The database is composed of 122 BUS images. 58 cases are benign and 64 cases are malignant confirmed by pathology. The images were collected by the doctors of the Second Affiliated Hospital of Harbin Medical University (Harbin, China), using a VIVID 7 (GE, Horten, Norway) with a 5–14 MHz linear probe. Informed consent to the protocol was obtained from all patients in the study, and the privacy of the patients was well protected. Every lesion is outlined by an experienced radiologist and the manual delineation is served as the reference standard.

To estimate the difficulty of the database, three experienced radiologists (with more than three years experience in sonography) carried out an experiment. For every case in the database, if all the three radiologists made the same correct diagnosis (benign/malignant), the case is considered as easy (typical); if one radiologist made wrong diagnosis, the case is considered as average; if two radiologists made wrong diagnosis, the case is considered as difficult; if all three radiologists made wrong diagnosis, the case is considered as very difficult. For the 122 cases in our database, 49 are easy, 42 are average, 22 are difficult, and 9 are very difficult.

III.B. Evaluation metrics

III.B.1. Area error metrics

Area error metrics can evaluate how much the lesion region is covered by the generated lesion region correctly and how much is covered wrongly. The true positive (TP) area ratio, the false positive (FP) area ratio, the false negative (FN) area ratio,⁶ and the similarity (SI) (Ref. 19) will be calculated:

$$\text{TP Area Ratio} = \frac{|A_m \cap A_a|}{|A_m|}, \quad (26)$$

$$\text{FP Area Ratio} = \frac{|A_m \cup A_a - A_m|}{|A_m|}, \quad (27)$$

$$\text{FN Area Ratio} = 1 - \text{TP Area Ratio} = \frac{|A_m \cup A_a - A_a|}{|A_m|}, \quad (28)$$

$$\text{SI} = \frac{|A_m \cap A_a|}{|A_m \cup A_a|}. \quad (29)$$

Here A_a is the pixel set of the automatically generated lesion region by the proposed method, and A_m is the pixel set of the manually outlined lesion region by the radiologist. Figure 5 shows the areas corresponding to TP, FP, and FN, respectively. SI measures how much the computer generated lesion region is similar to the radiologist's delineation, which

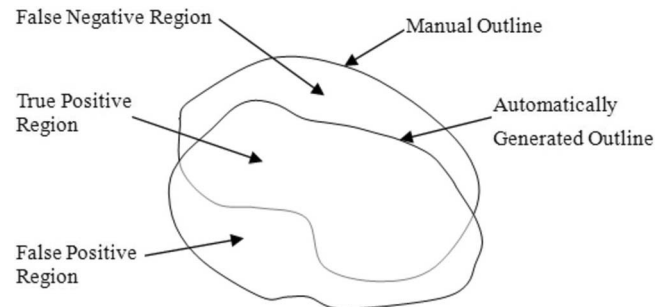


FIG. 5. Areas corresponding to TP, FP, and FN regions.

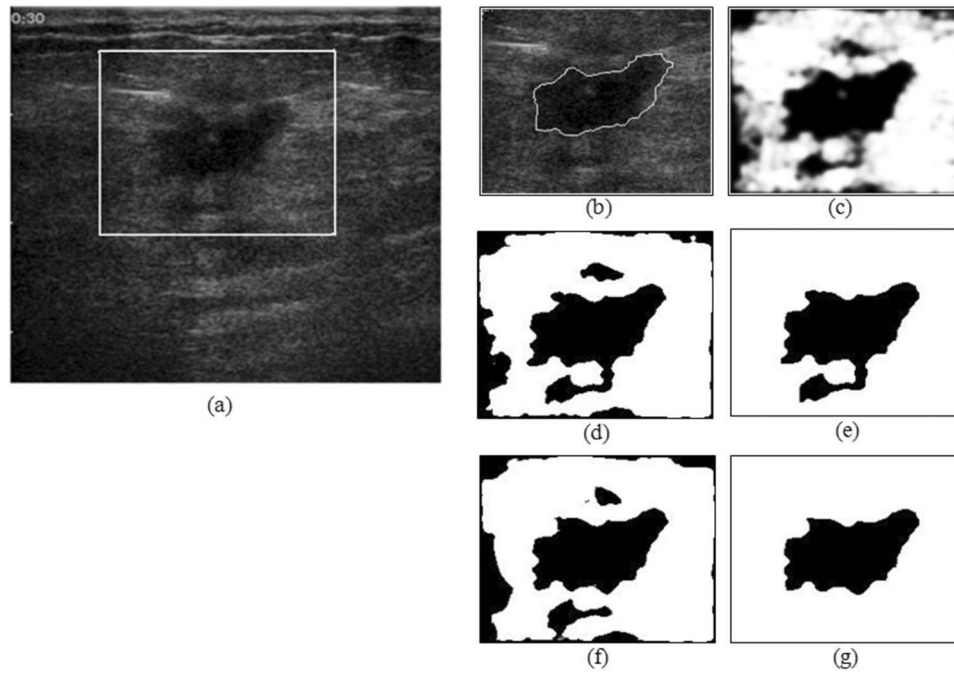


FIG. 6. (a) ROI. (b) Manually delineation by radiologist. (c) Enhanced PMO image. (d) Output of FCM. (e) Output of FCM after postprocessing. (f) Output of NLM. (g) Output of NLM after postprocessing.

is an overall performance evaluation. Mathematically, there is no need to list FN area ratio since $FN = 1 - TP$.

III.B.2. Boundary error metrics

We use two boundary error metrics to analyze the difference between the contours generated by the proposed ap-

proach and the contours marked by the radiologist. The two error metrics are Hausdorff distance (HD) (Ref. 38) and mean absolute distance (MD).⁶ We denote the manually delineated boundary as $Q = \{q_1, q_2, \dots, q_\gamma\}$ and the computer segmented result as $P = \{p_1, p_2, \dots, p_\mu\}$, and each element of Q or P is a point on the corresponding contour. We find the distances of every point in P to all the points in Q , and define

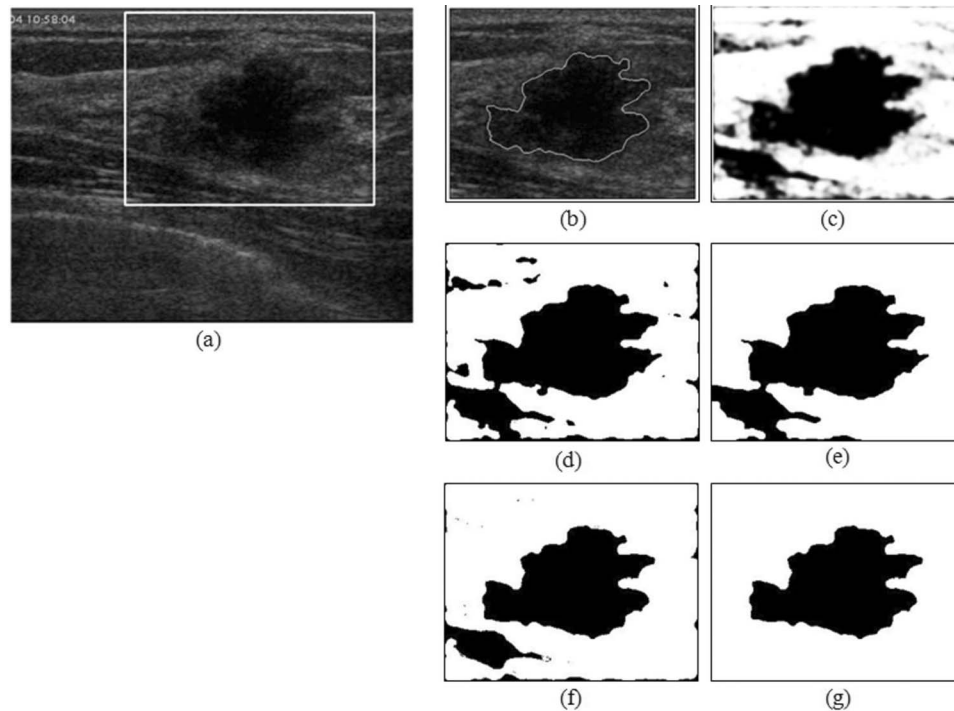


FIG. 7. (a) ROI. (b) Manually delineation by radiologist. (c) Enhanced PMO image. (d) Output of FCM. (e) Output of FCM after postprocessing. (f) Output of NLM. (g) Output of NLM after postprocessing.

TABLE I. Compare NLM with FCM.

Methods	Average area error metrics			Average boundary error metrics		
	TP(%)	FP(%)	SI(%)	Avg. HD	Avg. MD	Average time/case
FCM	87.2 ± 10.6	10.2 ± 15.7	79.7 ± 9.2	34.6 ± 22.0	8.0 ± 4.9	3.8 s
NLM	92.4 ± 6.5	7.2 ± 5.1	86.3 ± 5.5	22.5 ± 12.9	4.8 ± 2.4	5.2 s
<i>P</i> -value	<0.025	<0.005	<0.005	<0.005	<0.005	NA

Note: The unit for HD and MD is pixel. 1 pixel is approximately 0.35 mm for the image of DPI = 72 pixels/in. in the database.

the shortest distance of p_j to contour Q as

$$\forall p_j \in P, j = 1, \dots, \mu, \text{ we find} \\ d(p_j, Q) = \min_w \|p_j - q_w\|, w = 1, \dots, \gamma. \quad (30)$$

Similarly, we find the distances of every point in Q to all the points in P , and define the shortest distance of q_w to contour P as

$$\forall q_w \in Q, w = 1, \dots, \gamma, \text{ we find} \\ d(q_w, P) = \min \|q_w - p_j\|, j = 1, \dots, \mu, \quad (31)$$

where $\|\cdot\|$ is 2D Euclidean distance. HD and MD are defined as

$$\text{HD} = \max(\max_j d(p_j, Q), \max_w d(q_w, P)), \quad (32)$$

$$\text{MD} = \left(\frac{\sum_{j=1}^{\mu} d(p_j, Q)}{\mu} + \frac{\sum_{w=1}^{\gamma} d(q_w, P)}{\gamma} \right) / 2. \quad (33)$$

HD measures the worst possible disagreement between two contours while the MD measures the averaged disagreement over the two boundaries.

III.C. Compare NLM with FCM

First, we compare NLM with FCM using the same database. Every preprocessing step is carried out exactly the

same before applying NLM or FCM. And the same postprocessing operation of removing noisy regions is also applied for both NLM and FCM. Figures 6 and 7 show two examples of the outputs of NLM and FCM.

The major advantage of NLM over FCM is that NLM can deal with indeterminate regions effectively and accurately. As Fig. 6 shows, based on the neighborhood information, NLM incorporates the indeterminate regions into background. But FCM misclassifies the indeterminate regions into foreground, since it uses only the distance to calculate the cluster centers (membership is based on distance too), without considering the indeterminate degree. Another advantage of NLM is that it can smooth the complex background; therefore, it can prevent the lesion region from connecting with false foregrounds. Figure 7 shows such an example. Lesion region obtained by NLM [Fig. 7(f)] is not connected with any dark region in the background. Therefore, after simple postprocessing, the lesion boundary obtained by NLM is quite clear and accurate [Fig. 7(g)]. On the contrary, the output of FCM [Fig. 7(d)] has many noisy regions. Although we apply the same postprocessing operation to FCM, the lesion still misconnects with one of the false foreground regions [Fig. 7(e)]. Statistically, 20% of the images in the database have the misconnection problem by using FCM. The evaluation results of the average performance of both FCM and NLM on the entire database are listed in Table I.

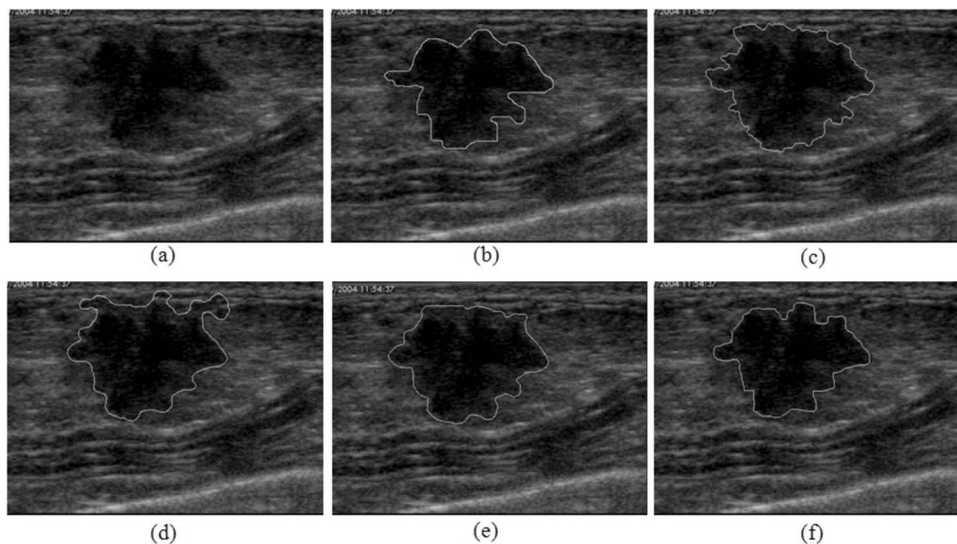


FIG. 8. (a) Original image. (b) Manual delineation by radiologist. (c) Output of the method given in Ref. 6. (d) Output of the method given in Ref. 19. (e) Output of the method given in Ref. 36. (f) Output of the proposed method.

TABLE II. Compare the proposed method with methods given in Refs. 6, 19, and 36.

Methods	Average area error metrics			Average boundary error metrics		
	TP(%)	FP(%)	SI(%)	Avg. HD	Avg. MD	Average time/case
Method given in Ref. 6	88.5 \pm 13.2	7.2 \pm 6.6	82.6 \pm 11.6	26.5 \pm 15.8	6.2 \pm 5.1	22.6 s
Method given in Ref. 19	91.6 \pm 7.5	13.1 \pm 43.8	84.0 \pm 10.1	31.9 \pm 23.4	6.2 \pm 4.5	58.0 s
Method given in Ref. 36	88.7 \pm 19.2	18.1 \pm 25.7	77.6 \pm 17.4	38.0 \pm 42.6	11.5 \pm 20.0	8.1 s
Proposed method	92.4 \pm 6.5	7.2 \pm 5.1	86.3 \pm 5.5	22.5 \pm 12.9	4.8 \pm 2.4	9.8 s

Note: The unit for HD and MD is pixel. 1 pixel is approximately 0.35 mm for the image of DPI = 72 pixels/in. in the database.

As Table I shows the average performance of NLM is much better than the average performance of FCM in all the evaluation metrics, using the entire database. Standard deviation and P -value for each metric are also listed. In statistics, if P -value ≤ 0.01 , the difference is considered highly significant. If $0.01 < P$ -value ≤ 0.05 , the difference is considered significant. The differences between the evaluation results of NLM and FCM are all significant (most of them are highly significant). The higher TP rate (improved from 87.2% to 92.4%) indicates that NLM covers more lesion region than FCM. The lower FP rate (decreased from 10.2% to 7.2%) indicates less miscoverage of the nonlesion regions. SI is an overall evaluation of the similarity between two regions. An improvement from 79.7% to 86.3% is quite remarkable, since P -value is less than 0.005, indicating highly significant difference. The better performance of NLM is illustrated by the boundary error metrics too. Here, we want to emphasize that the average Hausdorff distance (measuring the worst point-distance between two contours) is reduced from 34.6 pixels to 22.5 pixels, and the average mean distance is reduced from 8.0 pixels to 4.8 pixels, which means that the contours generated by NLM are much closer to the manual delineations. The processing time of FCM (3.8 s)

is faster than that of NLM (5.2 s). The longer processing time is mostly used for computing the neutrosophic components of each pixel; however, it makes the clustering process more precise, and such time is quite acceptable for clinic applications.

III.D. Compare the proposed method with other BUS segmentation methods

In this section, we compare the proposed method with three automatic segmentation methods for BUS images. The first one is an active-contour-based method which used low-level texture information to find the points on boundary, and employed an active contour model to detect the final lesion boundary;⁶ the second one is a level-set based method,¹⁹ combining both global statistical information and local edge information; and the third is a watershed-based segmentation method using neutrosophy.³⁶ The parameters used in these methods are well tuned. For example, the parameters α_{near} and α_{far} of the active contour method⁶ were tuned; the size of initial rectangle for the level-set method¹⁹ was tuned; and the parameters of mask size and filter in the watershed method³⁶ were tuned as well.

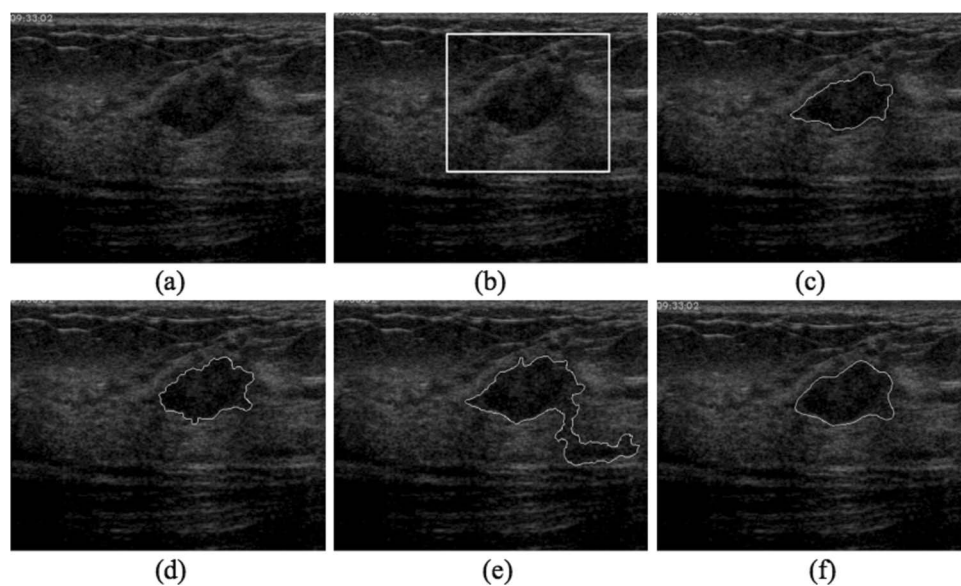


FIG. 9. (a) Original image with posterior shadows. (b) ROI generated by the proposed method. (c) Output of the proposed method. (d) Output of the active contour method given in Ref. 6. (e) Output of the level-set method given in Ref. 19. (f) Output of the watershed method given in Ref. 36.

TABLE III. Performance and standard deviation for different values of m .

m	Average area error metrics			Average boundary error metrics	
	TP(%)	FP(%)	SI(%)	Avg. HD	Avg. MD
2	92.41	7.21	86.27	22.51	4.78
3	92.37	7.08	85.92	22.93	4.83
4	92.62	7.35	86.22	23.02	4.92
5	92.23	7.13	86.20	22.78	4.86
Std	0.16	0.12	0.16	0.22	0.06

Note: The unit for HD and MD is pixel. 1 pixel is approximately 0.35 mm for the image of DPI = 72 pixels/in. in the database.

In Fig. 8, an example of the segmentation results of the four methods is provided. Figure 8(a) is the original image. Figure 8(b) is the manual delineation by a radiologist. Figures 8(c)–8(f) are the segmentation results of the active contour method,⁶ the level-set method,¹⁹ the watershed method,³⁶ and the proposed method, respectively. The lesion boundary detected by the proposed method is much closer to radiologist's manual delineation and more reasonable than that of the other three methods.

The average performances of the four methods are evaluated using the entire database too. Table II lists the accuracies and time costs of the four methods. Please notice that the time reported in Table I is only for FCM and NLM stages; while the time reported in Table II is the total time of a segmentation method. Compared with the other three methods, the proposed method achieves the best TP, FP, and SI rates, the shortest HD and MD and smallest standard deviations. Processing time of the proposed method (9.8 s) is much faster than that of the active contour method (22.6 s) (Ref. 6) and that of the level-set based method (58.0 s).¹⁹ The watershed method (8.1 s) (Ref. 36) has the fastest processing speed; however, its accuracy is low. Taking every aspect into consideration, the proposed method achieves the best performance while keeping an efficient processing speed, compared with the other three methods.

III.E. Performance on cases with long posterior acoustic shadows

It is usually hard to separate lesions from posterior acoustic shadows since posterior shadows connect with lesions and have similar intensity values with that of the lesions. The proposed method can deal with posterior shadows well. First, the ROI generation method can catch the tiny intensity difference between lesion and shadow [by the dynamic threshold in Eq. (1)], and stop region growing when such a difference is detected. Contrast enhancement can further enlarge the difference between lesion and shadow, and NLM clustering method will gradually classify the shadow pixels into the background. The active contour method⁶ and watershed method³⁶ can separate lesions from posterior shadows on most cases, but the level-set method¹⁹ tends to fail in distinguishing the lesion from the shadows. In Fig. 9, we provide an example with long posterior acoustic shadow and show the contours generated by different methods.

IV. SENSITIVITY ANALYSIS

A method is robust, if its performance is almost insensitive to the variation of the parameters.³⁷ We conduct sensitivity analysis by varying the parameters used in the proposed method. The tunable parameters are m (for membership calculation), w (for the size of window), and λ (for the threshold of indeterminate value).

IV.A. Effect of tuning membership parameter m

The parameter m is used to calculate membership in Eq. (22). We vary m and compute the standard deviations (stds) of the area error and boundary error metrics. As Table III shows, none of the area error metrics' stds exceed 0.2% and all the boundary error metrics' stds are under 0.3 pixel, i.e., the proposed method is quite robust to parameter m .

IV.B. Effect of tuning window size w

The parameter w represents the window size used in NLM algorithm step 5. Different w values are chosen to calculate the stds. The small stds for all the evaluation metrics shown in Table IV demonstrate that the proposed method is robust to window size.

IV.C. Effect of tuning threshold λ

We tune indeterminacy threshold λ and record the evaluation results in Table V. The small stds for all the evaluation metrics soundly demonstrate that the proposed method is robust to parameter λ .

TABLE IV. Performance and standard deviation for different values of w .

w	Average area error metrics			Average boundary error metrics	
	TP(%)	FP(%)	SI(%)	Avg. HD	Avg. MD
3	92.43	7.52	86.05	23.32	4.86
5	92.41	7.21	86.27	22.51	4.78
7	92.11	7.73	85.68	23.67	5.02
9	92.08	7.84	85.52	24.08	5.21
Std	0.19	0.28	0.34	0.67	0.19

Note: The unit for HD and MD is pixel. 1 pixel is approximately 0.35 mm for the image of DPI = 72 pixels/in. in the database.

TABLE V. Performance and standard deviation for different values of λ .

λ	Average area error metrics			Average boundary error metrics	
	TP(%)	FP(%)	SI(%)	Avg. HD	Avg. MD
0.1	92.41	7.21	86.27	22.51	4.78
0.2	92.48	7.41	86.15	22.90	4.83
0.3	92.51	7.46	86.18	23.27	4.85
Std	0.05	0.13	0.06	0.38	0.04

Note: The unit for HD and MD is pixel. 1 pixel is approximately 0.35 mm for the image of DPI = 72 pixels/in. in the database.

V. CONCLUSIONS

In this paper, we have proposed a novel and fully automatic segmentation method for BUS images. It consists of automatic ROI generation, speckle reduction, contrast enhancement, and NLM clustering. NLM is a generalization of FCM that can be applied to pattern classification, machine learning, data mining, and related areas. In this paper, NLM is applied to BUS image segmentation to demonstrate its superiority. The advantages of the proposed method are summarized as

1. It is completely automatic.
2. It can find the accurate lesion boundary even for complicated and low-contrast BUS images.
3. It outperforms the fuzzy c-means clustering and other three BUS segmentation methods. Experiment is carried out using a common database and the performance is evaluated by a set of comprehensive criteria.
4. The analysis time of the proposed method is about 9.8 s for each case, which is much faster than the active contour method and the level-set method. It is quite acceptable for real-time clinical applications.
5. The proposed method is very robust.

One of the future works is moving to the next stage of a CAD system and developing a classifier that can distinguish benign and malignant lesions based on the features extracted from the segmentation result. Since one of the ultimate goals of segmentation is to improve the diagnosis accuracy of a CAD system, testing whether the final diagnosis accuracy can be improved is a practical and reasonable criterion to evaluate different segmentation algorithms. Another future direction is to extend the segmentation method to deal with cases with multiple lesions. Currently our database contains only single-lesion cases. After enlarging our database with multiple-lesion cases, we will modify the proposed ROI generation method to generate a ROI for each lesion in the image. Then for each ROI, we can run the segmentation method to generate the contour of every lesion in a BUS image.

^{a)}Electronic mail: juan.shan@aggiemail.usu.edu

^{b)}Author to whom correspondence should be addressed. Electronic mail: hengda.cheng@usu.edu; Telephone: 435-797-2054; Fax: 435-797-3265.

^{c)}Electronic mail: yuxuan.wang@aggiemail.usu.edu

¹H. D. Cheng, J. Shan, W. Ju, Y. Guo, and L. Zhang, "Automated breast cancer detection and classification using ultrasound images: A survey," *Pattern Recogn.* **43**(1), 299–317 (2010).

²A. Jemal, R. Siegel, J. Xu, and E. Ward, "Cancer Statistics 2010," *CA Cancer J. Clin.* **60**, 227–300 (2010).

³K. Drukker, M. L. Giger, K. Horsch, M. A. Kupinski, C. J. Vyborny, and E. B. Mendelson, "Computerized lesion detection on breast ultrasound," *Med. Phys.* **29**(7), 1438–1446 (2002).

⁴American-College-of-Radiology, *ACR Standards 2000–2001*, Reston, VA, 2000.

⁵J. A. Noble and D. Boukerroui, "Ultrasound image segmentation: A survey," *IEEE Trans. Med. Imaging* **25**(8), 987–1010 (2006).

⁶A. Madabhushi and D. N. Metaxas, "Combining low-, high-level and empirical domain knowledge for automated segmentation of ultrasonic breast lesions," *IEEE Trans. Med. Imaging* **22**(2), 155–169 (2003).

⁷S. Joo, Y. S. Yang, W. K. Moon, and H. C. Kim, "Computer-aided diagnosis of solid breast nodules: Use of an artificial neural network based on multiple sonographic features," *IEEE Trans. Med. Imaging* **23**(10), 1292–1300 (2004).

⁸C.-K. Yeh, Y.-S. Chen, W.-C. Fan, and Y.-Y. Liao, "A disk expansion segmentation method for ultrasonic breast lesions," *Pattern Recogn.* **42**(5), 596–606 (2009).

⁹K. V. Mogatadkala, K. D. Donohue, C. W. Piccoli, and F. Forsberg, "Detection of breast lesion regions in ultrasound images using wavelets and order statistics," *Med. Phys.* **33**(4), 840–849 (2006).

¹⁰C. Kotropoulos and I. Pitas, "Segmentation of ultrasonic images using support vector machines," *Pattern Recogn. Lett.* **24**(4–5), 715–727 (2003).

¹¹Y. Zhan and D. Shen, "Deformable segmentation of 3D ultrasound prostate images using statistical texture matching method," *IEEE Trans. Med. Imaging* **25**(3), 256–272 (2006).

¹²H.-M. Wu and H. H.-S. Lu, "Iterative sliced inverse regression for segmentation of ultrasound and MR images," *Pattern Recogn.* **40**(12), 3492–3502 (2007).

¹³Y. Ikeda, D. Fukuoka, T. Hara, H. Fujita, E. Takada, T. Endo, and T. Morita, "Development of a fully automatic scheme for detection of masses in whole breast ultrasound images," *Med. Phys.* **34**(11), 4378–4388 (2007).

¹⁴Y.-L. Huang and D.-R. Chen, "Watershed segmentation for breast tumor in 2D sonography," *Ultrasound Med. Biol.* **30**(5), 625–632 (2004).

¹⁵W. Gomez, L. Leija, A. V. Alvarenga, A. F. C. Infantosi, and W. C. A. Pereira, "Computerized lesion segmentation of breast ultrasound based on marker-controlled watershed transformation," *Med. Phys.* **37**(1), 82–95 (2010).

¹⁶C.-M. Chen, Y.-H. Chou, C. S. K. Chen, J.-Z. Cheng, Y.-F. Ou, F.-C. Yeh, and K.-W. Chen, "Cell-competition algorithm: A new segmentation algorithm for multiple objects with irregular boundaries in ultrasound images," *Ultrasound Med. Biol.* **31**(12), 1647–1664 (2005).

¹⁷J.-Z. Cheng, Y.-H. Chou, C.-S. Huang, Y.-C. Chang, C.-M. Tiu, F.-C. Yeh, K.-W. Chen, C.-H. Tsou, and C.-M. Chen, "ACCOMP: Augmented cell competition algorithm for breast lesion demarcation in sonography," *Med. Phys.* **37**(12), 6240–6252 (2010).

¹⁸R. F. Chang, W. J. Wu, W. K. Moon, and D. R. Chen, "Automatic ultrasound segmentation and morphology based diagnosis of solid breast tumors," *Breast Cancer Res. Treat.* **89**(2), 179–185 (2005).

¹⁹B. Liu, H. D. Cheng, J. Huang, J. Tian, J. Liu, and X. Tang, "Automated segmentation of ultrasonic breast lesions using statistical texture classification and active contour based on probability distance," *Ultrasound Med. Biol.* **35**(8), 1309–1324 (2009).

²⁰R.-F. Chang, W.-J. Wu, W. K. Moon, W.-M. Chen, W. Lee, and D.-R. Chen, "Segmentation of breast tumor in three-dimensional ultrasound images using three-dimensional discrete active contour model," *Ultrasound Med. Biol.* **29**(11), 1571–1581 (2003).

²¹D.-R. Chen, R.-F. Chang, W.-J. Wu, W. K. Moon, and W.-L. Wu, "3D breast ultrasound segmentation using active contour model," *Ultrasound Med. Biol.* **29**(7), 1017–1026 (2003).

²²J. Cui, B. Sahiner, H.-P. Chan, A. Nees, C. Paramagul, L. M. Hadjiiski, C. Zhou, and J. Shi, "A new automated method for the segmentation and characterization of breast masses on ultrasound images," *Med. Phys.* **36**(5), 1553–1565 (2009).

²³D. Boukerroui, A. Baskurt, J. A. Noble, and O. Basset, "Segmentation of ultrasound images—multiresolution 2D and 3D algorithm based on global and local statistics," *Pattern Recogn. Lett.* **24**(4–5), 779–790 (2003).

²⁴G. Xiao, M. Brady, J. A. Noble, and Y. Zhang, "Segmentation of ultrasound B-mode images with intensity inhomogeneity correction," *IEEE Trans. Med. Imaging* **21**(1), 48–57 (2002).

- ²⁵M. H. Yap, E. A. Edirisinghe, and H. E. Bez, "A novel algorithm for initial lesion detection in ultrasound breast images," *J. Appl. Clin. Med. Phys.* **9**, 2741 (2008).
- ²⁶J. Shan, H. D. Cheng, and Y. Wang, "A novel automatic seed point selection algorithm for breast ultrasound images," *19th International Conference on Pattern Recognition in 2008 (ICPR, 2008)*.
- ²⁷Y. Yu and S. T. Acton, "Speckle reducing anisotropic diffusion," *IEEE Trans. Image Process.* **11**(11), 1260–1270 (2002).
- ²⁸J. Shan, H. D. Cheng, Y. Wang, J. Shan, H. D. Cheng, and Y. X. Wang, "Completely automated segmentation approach for breast ultrasound images using multiple-domain features," *Ultrasound Med. Biol.* **38**(2), 262–275 (2012).
- ²⁹P. Kovesi, "Phase congruency: A low-level image invariant," *Psychol. Res.* **64**(2), 136–148 (2000).
- ³⁰J. C. Dunn, "A fuzzy relative of the ISODATA process and its use in detecting compact well-separated clusters," *J. Cybern.* **3**(3), 32–57 (1973).
- ³¹J. Bezdek, *Pattern Recognition with Fuzzy Objective Function Algorithms* (Kluwer Academic Publishers, MA, 1981).
- ³²F. Smarandache, *A Unifying Field in Logics: Neutrosophic Logic. Neutrosophy, Neutrosophic Set, Neutrosophic Probability*, 3rd. ed. (American Research Press, Rehoboth, 2003).
- ³³H. D. Cheng and Y. Guo, "A new neutrosophic approach to image thresholding," *New Math. Nat. Comput.* **4**, 291–308 (2008).
- ³⁴L. A. Zadeh, "Fuzzy sets," *Inform. Control* **8**(3), 338–353 (1965).
- ³⁵Y. Guo and H. D. Cheng, "New neutrosophic approach to image segmentation," *Pattern Recogn.* **42**, 587–595 (2009).
- ³⁶M. Zhang, L. Zhang, and H. D. Cheng, "A neutrosophic approach to image segmentation based on watershed method," *Signal Process.* **90**(5), 1510–1517 (2010).
- ³⁷J. K. Udupa, V. R. LaBlanc, H. Schmidt, C. Imielinska, P. K. Saha, G. J. Grevera, Y. Zhuge, L. M. Currie, P. Molholt, and Y. Jin, *Methodology for Evaluating Image-Segmentation Algorithms* (SPIE, San Diego, CA, 2002).
- ³⁸D. P. Huttenlocher, G. A. Klanderman, and W. J. Rucklidge, "Comparing images using the Hausdorff distance," *IEEE Trans. Pattern Anal. Mach. Intell.* **15**, 850–863 (1993).